Dalton Transactions

ROYAL SOCIETY OF CHEMISTRY

PAPER

View Article Online
View Journal | View Issue

Check for updates

Cite this: *Dalton Trans.*, 2026, **55**, 3002

Effects of labile ligands and substituents in nickel enolate catalysts on ethylene/acrylate copolymerization activity: a DFT study

Ying Wang,[a,b] Xiaowei Xu,[a] Yi Luo,[a] Sicong Liu,[a] Zhuozheng Wang,[a] Hao Li,[a] Fan Yang,*[b] Xingxun Li*[b] and Weisheng Yang*[a]

Received 18th September 2025,
Accepted 6th January 2026

DOI: 10.1039/d5dt02237a

rsc.li/dalton

In this study, density functional theory (DFT) was employed to investigate the copolymerization mechanism of ethylene with *tert*-butyl acrylate (*t*BA) catalyzed by neutral nickel enolate complexes featuring distinct substituents. It is computationally found that [2,6-$(PhO)_2C_6H_3$]$_2$PCHC(Ph)O–Ni (**A**) is more active than [2,6-$(MeO)_2C_6H_3$]$_2$PCHC(Ph)O–Ni (**B**), which is in line with experimental observations. Based on this agreement, it is demonstrated that the ethylene insertion into the *t*BA chain-end is the rate-determining step and the activity discrepancy between **A** and **B** is closely associated with the electronic effects of the substituents rather than the difference in sterics between the PhO group in **A** and the MeO in **B**. The natural population analysis (NPA) indicates that the phenoxy substituent can more effectively increase the positive charge on the Ni center, thereby enhancing its copolymerization activity. The influence of the labile ligand (L) (L = pyridine, PEt_3 and PPh_3) on the copolymerization activity of the more active **A** has been further investigated. The coordination strength of the labile ligand was found to significantly influence the catalytic performance. Specifically, a weaker coordinating labile ligand facilitates the ligand exchange between L and the monomer (*t*BA and ethylene) and enhances the efficiency of chain propagation. These mechanistic insights are helpful for the molecular design of copolymerization catalysts with high performance.

1. Introduction

The copolymerization of polar and non-polar olefins has become a prominent research direction in the field of polyolefins. The incorporation of polar monomers into polyolefins through coordination copolymerization enables better control of their microstructures and material properties, thereby widening the range of their potential applications in packaging materials, automotive components, and electronic materials.[1–3] While early transition metal catalysts (*e.g.*, group 4 metallocenes) exhibit high activity for ethylene polymerization, their intolerance to polar functional groups severely limits their application in copolymerization reactions with polar monomers.[4–8] In contrast, late transition metal catalysts for the polymerization of polar olefins[9–17] (Fig. 1a) have been extensively studied in both academia and industry due to their low oxophilicity and excellent functional group tolerance.[18–25] However, highly efficient catalytic systems capable of addressing the copolymerization of polar and non-polar monomers on an industrial scale have been still limited. Among various catalytic options,[2,26,27] nickel catalysts are more attractive for industrial applications owing to their higher economic advantages, greater abundant resources, and superior catalytic activity in the homopolymerization of ethylene.[28,29] Notably, neutral phosphine–enolate nickel catalysts represent a versatile class of systems where steric and electronic modifications profoundly influence reactivity. Yet, the mechanistic basis of these effects, especially in acrylate copolymerization, has remained unclear, hindering rational catalyst design.

To develop the field of late transition metal catalyzed olefin copolymerization, researchers have explored various factors influencing catalyst performance. These include electronic effects, steric hindrance, and metal center characteristics.[30–39] Although notable progress has been achieved,[40] considerable challenges still remain in this research field.[41–43] A breakthrough was recently reported by Agapie *et al.*,[44] through the development of neutral nickel phosphine–enolate complexes, *viz.*, [2,6-$(PhO)_2C_6H_3$]$_2$PCHC(Ph)O–Ni (**A**) and [2,6-$(MeO)_2C_6H_3$]$_2$PCHC(Ph)O–Ni (**B**) (Fig. 1b). These complexes showed great potential in the coordination copolymerization of ethylene with *tert*-butyl acrylate (*t*BA). Remarkably, both

[a]*PetroChina Petrochemical Research Institute, Beijing 102206, China. E-mail: yangweisheng@petrochina.com.cn*
[b]*State Key Laboratory of Heavy Oil Processing, China University of Petroleum-Beijing, Beijing 102249, China*

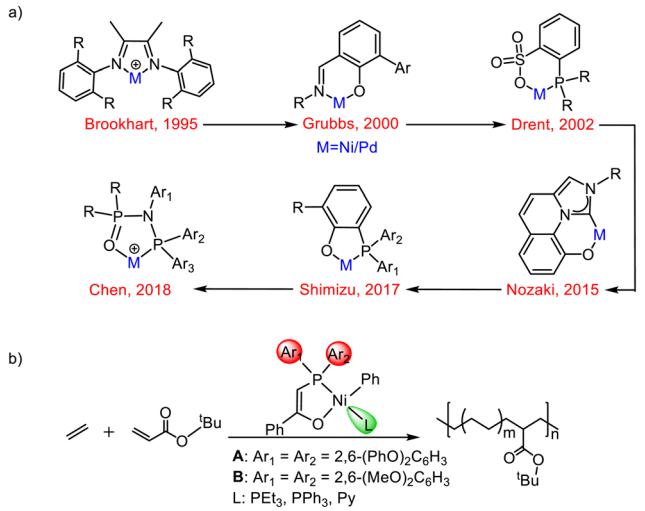

Fig. 1 (a) Examples of catalysts for copolymerization of ethylene and polar monomers. An alkyl group connected to the metal is omitted for clarity. (b) Copolymerization of ethylene with *t*BA catalyzed by nickel enolate catalysts in the presence of different labile ligands (L).

catalytic activity and thermal stability were substantially improved by strategically incorporating steric hindrance on the phosphine side of the asymmetric ligands. In subsequent work, the effect of labile ligand L on the ethylene/acrylate copolymerization process was investigated.[45] A 4–5 fold activity increase was observed when PEt_3 was replaced by pyridine (Py). This ligand modification strategy, being more feasible than backbone restructuring, provides an efficient approach for catalyst optimization.

This study employs DFT calculations to elucidate the mechanism of ethylene and *t*BA copolymerization catalyzed by neutral nickel phosphine–enolate complexes. The theoretical calculations reveal the regulatory effects of different substituents on the ethylene/*t*BA copolymerization activity and the influence mechanism of labile ligand L on the copolymerization performance at the molecular level (Fig. 1b). By providing a detailed understanding of the catalytic mechanism, this study aims to guide the rational design of more efficient and robust nickel catalysts for the copolymerization of polar and non-polar monomers, thereby addressing the current challenges in this field.

2. Computational details

All the density functional theory (DFT) calculations were performed using the Gaussian 16 program.[46] The TPSSTPSS[47] functional together with the 6-31G(d) basis set for nonmetal atoms (C, H, O, N, and P) and the LANL2DZ[48–50] basis set as well as associated pseudopotential for the metal atom (Ni) was used for geometry optimizations and subsequent frequency calculations. Such basis sets are denoted as BSI. Based on the TPSSTPSS/BSI geometries, single-point calculations were further performed at the higher level of theory by using the dispersion-corrected density functional method TPSSTPSS-D3BJ[51] together with BSII. In BSII, Def2-TZVP[52,53] was used for all the atoms. In these single-point calculations, the solvation effect of toluene (ε = 2.37) was considered through the SMD[54] model. The energy profiles were constructed at the TPSSTPSS-D3BJ/BSII(SMD)//TPSSTPSS/BSI level, including Gibbs free energy corrections taken from frequency calculations in the gas-phase (298.15 K, 1 atm). After carrying out the above calculations, the noncovalent interaction (NCI) analysis[55] was conducted for some important transition structures (TSs), which were shown using Multiwfn[56,57] and VMD[58] software. The optimized geometrical structures were plotted using CYLView.[59]

3. Results and discussion

To comparatively investigate the substituent effect, both phosphine enolate based catalysts **A** and **B** are selected as computational models in this study, as shown in Chart 1, for a systematic mechanistic exploration of their coordination–insertion processes. The two catalysts exhibit distinct electronic and structural properties. The nickel center in catalyst **A** shows a higher NPA charge compared to that in catalyst **B** (+0.121 *vs.* +0.071), indicating stronger electron inadequacy. Structurally, catalyst **A** exhibits a larger dihedral angle (P_2–Ni–O_1–C_1 = −10.1°) than catalyst **B** (−8.5°), suggesting greater flexibility. These differences might contribute to their distinct catalytic activities.[44]

3.1 Copolymerization mechanism of ethylene and *t*BA

Due to the electronic asymmetry of the ancillary ligand, the vinyl monomer may show two spatial orientations during coordination insertion: *trans* site (monomer in *trans* configuration to the phosphorus atom) and *cis* site (monomer in *cis* configuration to the phosphorus atom). Previous studies[60–63] have demonstrated that the *cis*-site coordination is less stable than the *trans*-site ($\Delta G_{cis} > \Delta G_{trans}$), but its insertion energy barrier is significantly lower than that of the *trans*-site ($\Delta G^{\ddagger}_{cis} < \Delta G^{\ddagger}_{trans}$). Based on this theoretical understanding, this study focuses on the *cis*-site insertion pathway to reveal the microscopic mechanism of the most favorable reaction pathway.

As illustrated by the red pathway in Fig. 2, the chain initiation process catalyzed by **A-CAT** involves several critical elementary steps, beginning with ligand exchange:[21] ethylene coordinates to the active nickel center in a *trans*-coordination mode, while the weakly coordinating triethylphosphine (PEt_3) ligand dissociates from the metal center, yielding the *trans*-coordinated intermediate **A-C*t*$_1$**. This step requires overcoming an energy barrier of 27.5 kcal mol^{-1}, and the resulting *trans*-configuration in **A-C*t*$_1$** is stabilized by the combined electronic and steric effects of the nickel center, favoring initial coordination. Subsequently, **A-C*t*$_1$** undergoes a configuration flip to form the *cis*-coordinated intermediate **A-C*c*$_1$**, a step requiring an isomerization barrier of 30.6 kcal mol^{-1}. Ethylene then inserts through a four-center transition state **A-TS$_1$**, with an

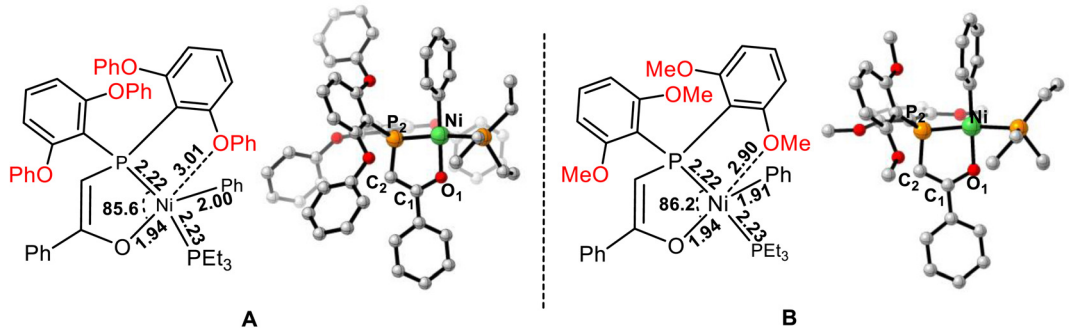

Chart 1 Optimized structures of complexes **A** and **B**. Hydrogen atoms are omitted for clarity.

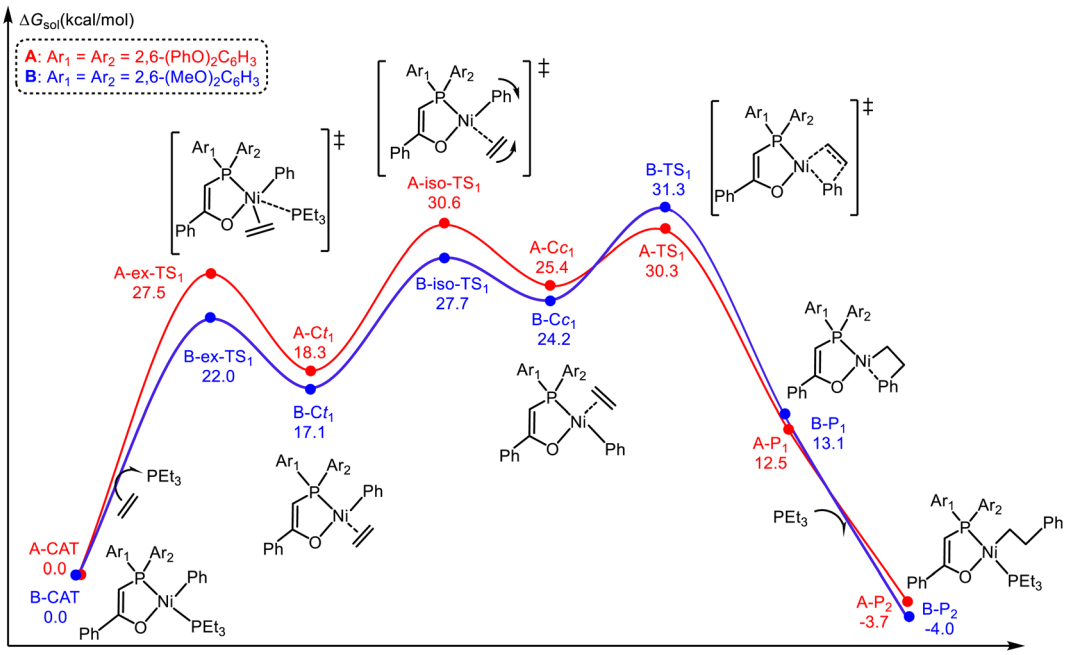

Fig. 2 Energy profile for the chain initiation in the **A** and **B** systems. The energies are relative to the corresponding reactants.

activation barrier of 30.3 kcal mol^{-1}, to afford the chain-initiation product **A-P$_1$**. Additionally, more detailed calculations on the ligand exchange and isomerization processes are provided in Fig. S1 and S2, offering further insights into these mechanisms. Similarly, catalyst system **B** (blue pathway in Fig. 2) follows the sequence: **B-CAT → B-ex-TS$_1$ → B-C*t*$_1$ → B-iso-TS$_1$ → B-C*c*$_1$ → B-TS$_1$ → B-P$_1$ → B-P$_2$**. In this pathway, the ligand-exchange barrier is 22.0 kcal mol^{-1}, the *trans*/*cis* isomerization barrier is 27.7 kcal mol^{-1}, and the ethylene insertion barrier is 31.3 kcal mol^{-1}. Overall, although the two catalytic systems follow similar reaction pathways, **A-CAT** exhibits lower activation barriers during the chain-initiation stage (30.6 *vs.* 31.3 kcal mol^{-1}).

Afterward, the insertion of *t*BA and subsequent ethylene insertion are further calculated. In the polar monomer insertion process of the **A** system, there are two types of *trans*-site coordination: one is the coordination of the carbonyl oxygen of the functional group to the metal center, and the other is the coordination of the C=C bond of the monomer to the metal center. Given that the product formed upon the insertion of the first ethylene molecule is in the *cis* configuration, the *trans* position is preferentially occupied when the polar monomer coordinates. Consequently, in the whole process of insertion of polar monomers, the primary insertion modes involve carbonyl oxygen *trans*-coordination, carbon–carbon double bond *trans*-coordination, and carbon–carbon double bond *cis*-coordination. Additionally, based on regioselectivity, the polar monomer insertion modes are categorized into 1,2-insertion and 2,1-insertion. As shown in Table 1, in the case of the **A** system, the energy barrier for 2,1-insertion is 3.7 kcal mol^{-1} lower than that for 1,2-insertion (28.9 *vs.* 32.6 kcal mol^{-1}), indicating a preference for the 2,1-insertion mode, which is common in such kind of systems.[35,64–66] The similar is true for the catalyst **B** system (26.2 *vs.* 32.8 kcal mol^{-1}).

Table 1 The calculated relative free energies in solution (ΔG, kcal mol^{-1}) for various insertions of *t*BA based on catalysts **A** and **B**[a]

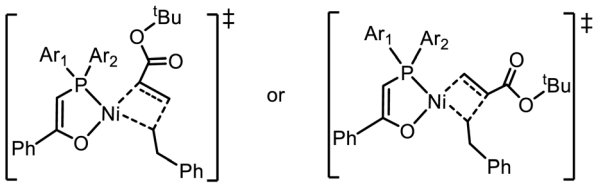

Catalyst	$\mathbf{P_2}$	**C*t*-O**	$^{1,2\text{-}t\text{BA}}$**C*t*2** ($^{2,1\text{-}t\text{BA}}$**C*t*2**)	$^{1,2\text{-}t\text{BA}}$**C*c*2** ($^{2,1\text{-}t\text{BA}}$**C*c*2**)	$^{1,2\text{-}t\text{BA}}$**TS2** ($^{2,1\text{-}t\text{BA}}$**TS2**)	$\Delta G^{\ddagger(1,2\text{-}t\text{BA})}$ ($\Delta G^{\ddagger(2,1\text{-}t\text{BA})}$)	$\Delta\Delta G^{\ddagger}$
A	−3.7	11.5	12.2 (12.5)	14.8 (14.6)	28.9 (25.2)	32.6 (28.9)	3.7
B	−4.0	12.1	10.2 (10.7)	13.5 (12.9)	28.8 (22.2)	32.8 (26.2)	6.6

[a] $\mathbf{P_2}$ denotes the insertion products with the ethylene chain-end. **C*t*-O** denotes the intermediate with carbonyl-coordinating *t*BA at the *trans*-site. **TS** represents the insertion transition states. **C*t*$_2$** and **C*c*$_2$** represent the coordination of *t*BA *via* its vinyl (C=C) at the *trans*-site and *cis*-site, respectively. $\Delta G^{\ddagger}$ represents the insertion free-energy barrier. The energies of the stationary points are relative to the corresponding catalyst and monomer.

Table 1 indicates the relative energies of the relevant regioselectivities during the insertion of polar monomers, showing that for catalyst **B**, the 2,1-insertion mode is equally dominant for *t*BA monomer insertion. Compared to **A-CAT**, **B-CAT** exhibits a lower energy barrier for *t*BA insertion. This is because **A-CAT** undergoes significant geometric distortion due to steric effects during the reaction, and the resulting distortion energy becomes the dominant factor whose unfavorable impact cannot be compensated by electronic effects, as demonstrated by the distortion/interaction analysis (Fig. S3).

The energy profiles for chain propagation are depicted in Fig. 3, with red traces representing the reaction pathways for catalyst **A** and blue traces for catalyst **B**. In system **A**, the ethylene insertion following *t*BA insertion is the rate-determining step in the chain growth process, with a reaction energy barrier 2.3 kcal mol^{-1} higher than that of the *t*BA insertion (31.2 *vs.* 28.9 kcal mol^{-1}). The similar is true for system **B** (32.5 *vs.* 26.2 kcal mol^{-1}). This phenomenon is primarily attributed to increased steric hindrance of the polymer chain and reduced nucleophilicity of the polymer chain resulting from the electron-withdrawing nature of the ester group.

As shown in Fig. 3, although catalyst **B** exhibits a lower energy barrier in the *t*BA insertion step compared with the **A** system, its higher energy barrier for subsequent ethylene insertion limits the overall reaction rate.[67,68] Both catalysts show higher energy barriers for the insertion of ethylene into the

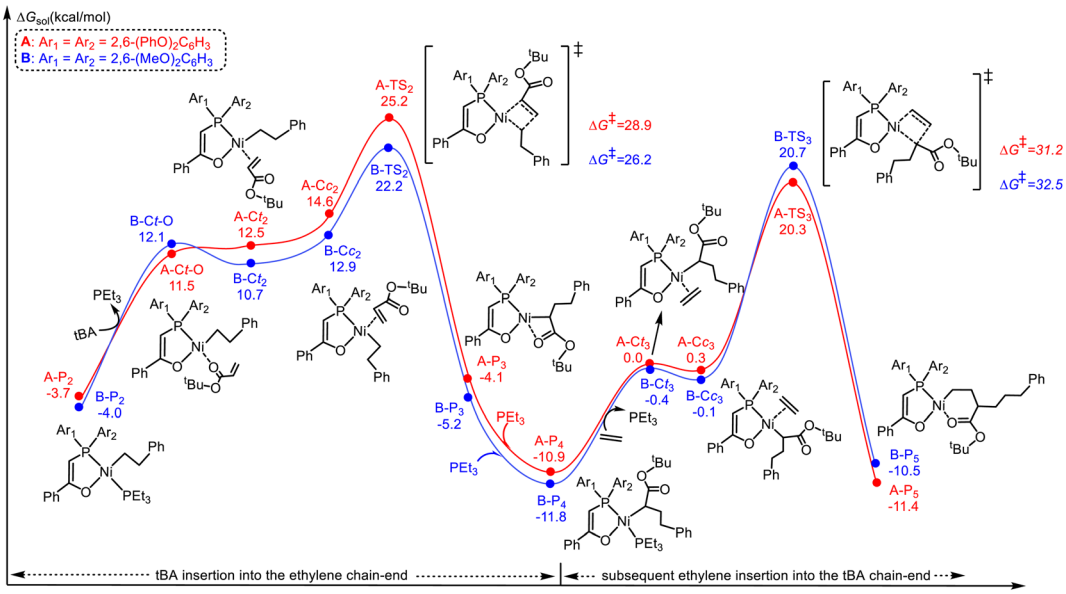

Fig. 3 Energy profile for chain propagation mediated by **A** and **B**, respectively, including *t*BA insertion into the ethylene chain-end and subsequent ethylene insertion into the *t*BA chain-end. The energies are relative to the corresponding reactants.

*t*BA chain-end compared with the insertion of *t*BA, which might be the key factor leading to the differences in copolymerization reaction rates. To ensure structural integrity, the pathways for ligand exchange and *trans*/*cis* isomerization during the chain propagation process are presented in Fig. S4 and S5. Computational results confirm that these isomeric processes have lower energy barriers than the rate-determining step. Given that the ground-state energies of intermediates $\mathbf{P_5}$ and $\mathbf{P_4}$ are similar, we further investigated the ethylene insertion reaction starting from $\mathbf{P_5}$. The results indicate that this subsequent ethylene insertion does not lead to a significantly higher energy barrier (Fig. S6). To ensure the reliability of DFT results, this study employed multiple DFT methods to evaluate single-point energies for key intermediates in the rate-determining step. All methods consistently indicated that catalyst **A** exhibits higher activity than catalyst **B** (Table S1). Subsequent studies will further investigate the influence of catalyst structure on the reaction energy barrier by integrating molecular orbital theory and distortion/interaction analysis.

3.2 Analyses of the factors governing the copolymerization activity

3.2.1 Effects of the substituents. Theoretical calculations reveal that catalyst **A** exhibits slightly higher polymerization activity than catalyst **B** (Fig. 3), which is consistent with experimental observations.[44] In order to investigate the main reason for the difference in catalytic activity between catalysts **A** and **B** in the copolymerization of ethylene and *t*BA, the energy profiles (Fig. 3) are carefully analyzed.

The structural and electronic properties of the catalysts dictate both the reaction pathways and their associated energy profiles. Natural population analysis (NPA) shows that the Ni center in $\mathbf{A\text{-}TS_3}$ carries a higher positive charge than in $\mathbf{B\text{-}TS_3}$ (+0.235 *vs.* +0.228). Such a higher positive charge (electronic effect) dominantly contributed to the higher stability of $\mathbf{A\text{-}TS_3}$, as also demonstrated by the distortion/interaction analysis (Fig. 4). According to the frontier molecular orbital theory, the highest occupied molecular orbital (HOMO) of ethylene interacts with the lowest unoccupied molecular orbital (LUMO) of enolate nickel catalysts during the reaction process. This interaction facilitates the transfer of electrons from the reactants to the catalysts. The LUMO energies of catalysts **A** and **B** are −3.718 eV and −3.506 eV, respectively. Compared to the HOMO orbital energy of ethylene (−6.335 eV), catalyst **A** exhibits better orbital overlap and therefore higher reactivity. This electronic advantage directly accounts for the superior activity of catalyst **A** in ethylene/*t*BA copolymerization. However, catalyst **A** demonstrates a higher activation energy barrier for *t*BA insertion (28.9 kcal mol^{-1} in **A** *vs.* 26.2 kcal mol^{-1} in **B**), which can be attributed to the larger axial spatial steric hindrance. While this steric effect improves catalyst stability, it may also cause overcrowding at the metal center, potentially hindering the insertion of bulky polar monomers. This trade-off between electronic and steric effects highlights the complex interplay of factors influencing the catalytic performance.

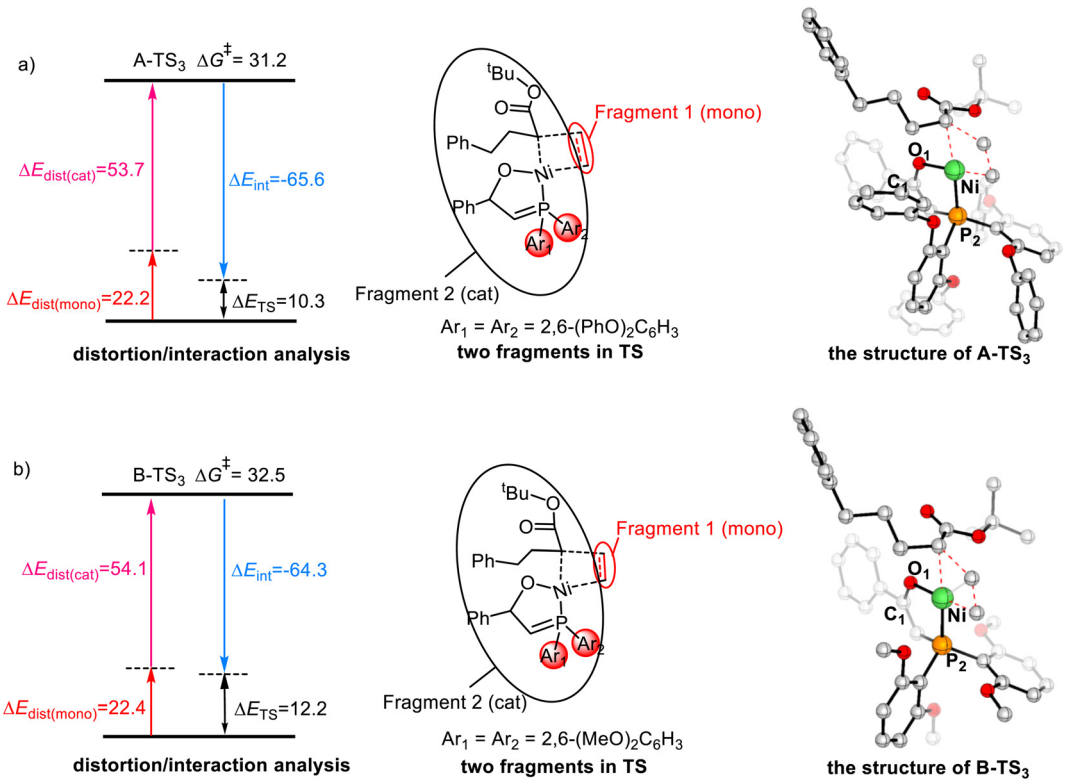

Fig. 4 The distortion/interaction analysis (energy in kcal mol^{-1}) and the optimized structures of (a) $\mathbf{A\text{-}TS_3}$ and (b) $\mathbf{B\text{-}TS_3}$.

To further explore and explain the reasons for the differences in copolymerization activity between the two catalysts, a distortion/interaction analysis is performed on the rate-determining transition states **A-TS$_3$** and **B-TS$_3$** (Fig. 4). In the distortion/interaction analysis, the energies of the monomer fragment and the remaining metal complex fragment (two fragments) in the transition state geometry are obtained through single-point calculations. The interaction energy (ΔE_{int}) in the transition state is calculated as the difference between the total energy of the transition state and the sum of the single-point energies of the two isolated fragments. The distortion energies of the two fragments, $\Delta E_{dist(cat)}$ and $\Delta E_{dist(mono)}$, are determined by comparing the energy of each fragment in the transition state geometry with its energy in its optimized geometry. Thus, the total electronic energy of the transition state is the sum of the interaction energy and the distortion energies, *i.e.*, $\Delta E_{TS} = \Delta E_{int} + \Delta E_{dist(cat)} + \Delta E_{dist(mono)}$.

As shown in Fig. 4, the distortion energy of the catalyst part in the transition state is labeled in pink ($\Delta E_{dist(cat)}$), while the distortion energy of the monomer part is labeled in red ($\Delta E_{dist(mono)}$). The calculated results reveal that in **A-TS$_3$**, the distortion energy of the monomer is 22.2 kcal mol^{-1}, and that of the catalyst fragment is 53.7 kcal mol^{-1}, yielding a total distortion energy of 75.9 kcal mol^{-1}. In contrast, for **B-TS$_3$**, the distortion energy of the monomer is 22.4 kcal mol^{-1}, and that of the catalyst fragment is 54.1 kcal mol^{-1}, resulting in a total distortion energy of 76.5 kcal mol^{-1}. In comparison, the total distortion energy of **A-TS$_3$** is lower than that of **B-TS$_3$** (75.9 *vs.* 76.5 kcal mol^{-1}), and this difference is reflected in the change of dihedral angle P_2–Ni–O_1–C_1 between catalysts **A** and **B**. Catalyst **A** exhibits a smaller change in the P_2–Ni–O_1–C_1 dihedral angle from −10.06° to −9.18°, whereas catalyst **B** undergoes a greater structural deformation (−8.52° → −5.33°), resulting in lower stability. This made catalyst **B** exhibit lower reactivity in catalyzing the copolymerization of *t*BA with ethylene. Furthermore, the stronger interaction between the monomer unit and the metal catalyst in **A-TS$_3$** (ΔE_{int} values of −65.6 and −64.3 kcal mol^{-1} for **A-TS$_3$** and **B-TS$_3$**, respectively) might originate from the weak van der Waals interactions between the benzene ring of the phenoxy substituent on the phosphorus and the alkyl chain or other benzene rings in catalyst **A** (Fig. S7). Such weak interactions, however, are absent in catalyst **B**, which might explain the weaker interaction between the two fragments in **B** compared to the one in catalyst **A**. A comparison of the contribution of deformation and interaction energies to the more stability of **A-TS$_3$** indicates that the interaction energy (electronic effect) is dominant (difference between **A-TS$_3$** and **B-TS$_3$**: deformation energy of – 0.6 kcal mol^{-1} *vs.* interaction energy of – 1.3 kcal mol^{-1}). The above multiscale theoretical analyses indicate that catalyst **A** exhibits smaller deformation energy and stronger interaction energy, which ultimately results in a more stable electronic energy of the transition state (ΔE_{TS} of 10.3 *vs.* 12.2 kcal mol^{-1}). These results indicate that catalyst **A** has higher activity in ethylene/*t*BA copolymerization. The strong agreement between these results and experimental observations provides a critical theoretical foundation for understanding the relationship between catalyst structure and performance.

3.2.2 Labile ligand effect. Typically, late transition metal catalysts such as Pd and Ni feature a bidentate ancillary ligand and a labile ligand (L). The labile ligand L plays a critical role in ethylene/*t*BA copolymerization activity. Given that catalyst **A** demonstrates higher activity in copolymerization, the influence of the labile ligand on catalytic performance has been further investigated on the basis of the catalyst **A** system.

DFT calculations revealed that the ligand-exchange process for different ligands L differs significantly, with the ligand-exchange energy ΔG_{ex} being 8.2 kcal mol^{-1} for pyridine (Py), 16.8 kcal mol^{-1} for triphenylphosphine (PPh_3), and 18.3 kcal mol^{-1} for triethylphosphine (PEt_3), as shown in Fig. 5. This establishes the stability trend in the order of Py < PPh_3 < PEt_3, which directly impacts catalytic behavior. Specifically, Py has a significantly higher propensity to undergo ligand exchange with ethylene than PEt_3 and PPh_3. This suggests that the Py ligand dissociates more easily from the metal center, thereby exposing the active site and reducing the energy barrier during the chain initiation stage (Fig. S8). To gain a deeper understanding of the mechanism by which the labile ligand influences the activity of catalyst **A**, we conducted frontier orbital analysis on three L-ligated catalyst systems: PEt_3 (**A-1**), PPh_3 (**A-2**), and pyridine (**A-3**). The results indicate that L significantly modulates the electronic structure, with HOMO–LUMO energy gaps of: **A-1** (2.37 eV) > **A-2** (2.11 eV) > **A-3** (1.93 eV). According to the chemical hardness theory[69,70] ($\eta = (E_{(LUMO)} - E_{(HOMO)})/2$), the **A-3** system with pyridine coordination has the lowest η value, indicating higher reactivity and greater propensity to participate in chemical reactions. These results agree with Xiong *et al.*'s work, confirming Py's advantages in reducing initiation barriers.[45] Furthermore, according to the NPA charge analysis, the charges on the metal center (Ni) in the three catalysts (**A-1**, **A-2**, and **A-3**) increase in the following order: **A-1** (0.121) < **A-2** (0.151) < **A-3** (0.267). These results indicate that the nature of the ligand (L) significantly influences the electrophilicity of the metal center (Ni), thereby modulating its catalytic activity. Specifically, the aromatic Py ring features electron delocalization and exhibits electron-withdrawing effects, which may reduce the electron density at the metal center (Ni) and results in a more positive charge (0.267 for **A-3**). In contrast, PPh_3 and PEt_3 have P atoms as strong electron donors, resulting in relatively lower positive charges on the metal center (Ni). This difference in charge distribution reflects the role of the labile ligand in modulating the elec-

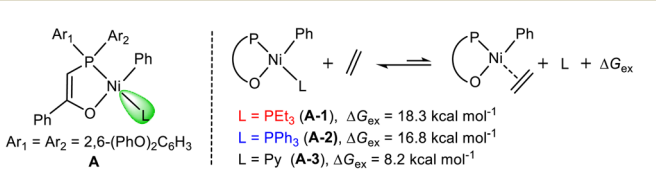

Fig. 5 Ligand exchange energetics (ΔG_{ex}) in catalyst **A** with three labile ligands.

Table 2 The calculated relative free energies in solution (ΔG, kcal mol^{-1}) for ethylene/*t*BA insertion in the catalyst **A** system with various labile ligands (L)[a]

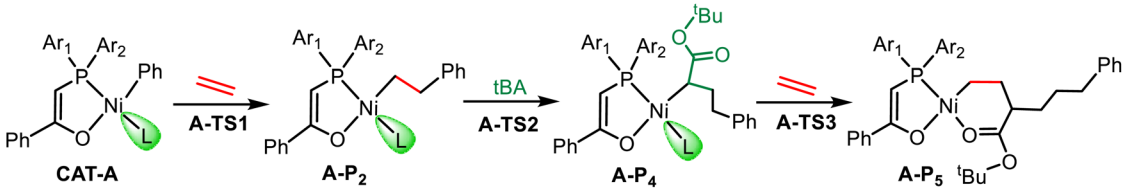

CAT	L	**A-TS$_1$**	**A-P$_2$**	**A_TS**	$\Delta G^{\ddagger}_{t\mathrm{BA}}$	**A-P$_4$**	**A_TS$_3$**	**A-P$_5$**	$\Delta G^{\ddagger}_{\mathrm{E}}$
A-1	PEt_3	30.3	−3.7	25.2	28.9	−10.9	20.3	−11.4	31.2
A-2	PPh_3	28.9	−6.5	23.8	30.3	−10.7	18.9	−12.8	29.6
A-3	Py	20.2	−8.3	15.1	23.4	−17.4	10.2	−21.4	27.6

[a] **A_TS$_1$**, **A_TS$_2$**, and **A_TS$_3$** represent the insertion transition states. **A-P$_2$** and **A-P$_4$** denote the insertion products with coordination of L, and **A-P$_5$** represents the insertion product of ethylene into the *t*BA chain-end. $\Delta G^{\ddagger}_{t\mathrm{BA}}$ and $\Delta G^{\ddagger}_{\mathrm{E}}$ represent the insertion free-energy barriers for *t*BA and ethylene, respectively. The energies of the stationary points are relative to the corresponding reactants. The corresponding complete energy profile is presented in Fig. S8 and S9.

tronic structure of the metal center, which in turn affects the overall performance of the catalyst.

We further examined the chain propagation process of the catalyst **A** system with the coordination of different ligands (L). After the insertion of one ethylene molecule, the resulting intermediate binds with ligand L to form a more stable **A-P$_2$** complex, followed by the insertion of polar monomers. As shown in Table 2, **A-3** shows the lowest insertion energy barrier at the rate-determining step (see Fig. S9 for the complete energy profile) due to the smallest exchange energy of Py. The smaller steric hindrance of the Py ligand allows *t*BA to more easily approach the metal center and insert, resulting in a lower energy barrier and a higher insertion rate of polar monomers in the case of **A-3**. In contrast, PPh_3 and PEt_3 exhibit larger steric hindrance, especially PPh_3, whose significant steric hindrance impedes the insertion of bulky polar monomers (*e.g.*, *t*BA), leading to the highest insertion energy barrier. As a result, **A-2** exhibits the highest energy barrier for *t*BA insertion among the three cases (28.9, 30.3, and 23.4 kcal mol^{-1} for **A-1**, **A-2**, and **A-3**, respectively). Both theoretical and experimental results demonstrate that the Py ligated catalyst **A-3** exhibits the highest copolymerization activity, while the PEt_3-ligated catalyst **A-1** and the PPh_3-ligated catalyst **A-2** show relatively lower activity due to their larger ligand-exchange energy. Although ligands with large steric hindrance (*e.g.*, PPh_3) can enhance catalyst stability, they might also hinder the insertion of bulky polar monomers. Therefore, when designing catalysts, the trade-off between steric hindrance of ligand L and catalytic activity could be necessary.

4. Conclusions

In summary, a comparative DFT study on the copolymerization mechanism of ethylene and *tert*-butyl acrylate (*t*BA) catalyzed by nickel enolate catalysts $[2,6\text{-}(PhO)_2C_6H_3]_2PCHC(Ph)O\text{–}Ni$ (**A**) and $[2,6\text{-}(MeO)_2C_6H_3]_2PCHC(Ph)O\text{–}Ni$ (**B**) is conducted, elucidating the influence mechanisms of the different substituents and labile ligands (L) on the copolymerization activity. It is found that the ethylene insertion into the *t*BA chain-end exhibits the highest reaction energy barrier, indicating that this step is the rate-determining step. The phenoxy substituent in catalyst **A** increases the positive charge on the Ni center dominantly through electronic effects, enhancing the interaction between the metal center and the monomer, thereby improving catalytic activity. The distortion/interaction analysis of the rate-determining step shows that catalyst **A** undergoes smaller geometric deformation in the transition state and exhibits stronger interaction, along with its weak interactions with surrounding atoms, which further stabilizes the transition state and reduces the reaction energy barrier. Based on the highly active catalyst **A**, the role of the labile ligands was investigated. In the catalytic process, monomers (ethylene or acrylates) must first replace ligand L and coordinate to the nickel center to undergo subsequent insertion reactions. The result reveals that the ligand exchange ability of the three labile ligands with monomers follows the order of Py > PPh_3 > PEt_3, which significantly influences the catalyst activity. Specifically, when the labile ligand is pyridine, catalyst **A** exhibits "fast initiation and slow growth" behavior. In contrast, with triethylphosphine (PEt_3) as the ligand, its stronger coordination ability leads to "slow initiation and slow growth" behavior, and the influence of L persists even after the initiation step. Consequently, catalyst **A** exhibits the highest activity when pyridine is used as the labile ligand.

Conflicts of interest

There are no conflicts to declare.

Data availability

All the relevant data are within the manuscript and its supplementary information (SI). The energy profiles mentioned in the main text, analyses of energies and NCI, as well as the optimized coordinates of the stationary points are available in SI. Supplementary information is available. See DOI: https://doi.org/10.1039/d5dt02237a.

References

1 L. Guo, W. Liu and C. Chen, *Mater. Chem. Front.*, 2017, **1**, 2487–2494.
2 R. Wu, W. K. Wu, L. Stieglitz, S. Gaan, B. Rieger and M. Heuberger, *Coord. Chem. Rev.*, 2023, **474**, 214844.
3 J. Y. Dong and Y. Hu, *Coord. Chem. Rev.*, 2005, **250**, 47–65.
4 H. Wang, Y. Yang, M. Nishiura, Y. Higaki, A. Takahara and Z. Hou, *J. Am. Chem. Soc.*, 2019, **141**, 3249–3257.
5 H. Nsiri, I. Belaid, P. Larini, J. Thuilliez, C. Boisson and L. Perrin, *ACS Catal.*, 2016, **6**, 1028–1036.
6 J. Chen, Y. Gao and T. J. Marks, *Angew. Chem., Int. Ed.*, 2020, **59**, 14726–14735.
7 C. Wu, M. Ren, L. Hou, S. Qu, X. Li, C. Zheng, J. Chen and W. Wang, *Engineering*, 2023, **30**, 93–99.
8 M. Atiqullah, M. Tinkl, R. Pfaendner, M. N. Akhtar and I. Hussain, *Polym. Rev.*, 2010, **50**, 178–230.
9 B. S. Xin, N. Sato, A. Tanna, Y. Oishi, Y. Konishi and F. Shimizu, *J. Am. Chem. Soc.*, 2017, **139**, 3611–3614.
10 M. Chen and C. Chen, *Angew. Chem., Int. Ed.*, 2018, **57**, 3094–3098.
11 X. Sui, S. Dai and C. Chen, *ACS Catal.*, 2015, **5**, 5932–5937.
12 B. P. Carrow and K. Nozaki, *J. Am. Chem. Soc.*, 2012, **134**, 8802–8805.
13 T. R. Younkin, E. F. Connor, J. I. Henderson, S. K. Friedrich, R. H. Grubbs and D. A. Bansleben, *Science*, 2000, **287**, 460–462.
14 L. K. Johnson, C. M. Killian and M. Brookhart, *J. Am. Chem. Soc.*, 1995, **117**, 6414–6415.
15 E. Drent, R. van Dijk, R. van Ginkel, B. van Oort and R. I. Pugh, *Chem. Commun.*, 2002, 744–745.
16 R. Nakano and K. Nozaki, *J. Am. Chem. Soc.*, 2015, **137**, 10934–10937.
17 W. Tao, R. Nakano, S. Ito and K. Nozaki, *Angew. Chem., Int. Ed.*, 2016, **55**, 2835–2839.
18 C. Chen, *ACS Catal.*, 2018, **8**, 5506–5514.
19 M. T. d. Costa, E. F. Lopes, R. S. Oliboni, D. S. Lüdtke, O. L. Casagrande and R. Stieler, *Appl. Organomet. Chem.*, 2023, **37**, e6984.
20 J. Ye, H. Mu, Z. Wang and Z. Jian, *Organometallics*, 2019, **38**, 2990–2997.
21 M. M. Shoshani, S. Xiong, J. J. Lawniczak, X. Zhang, T. F. Miller and T. Agapie, *Organometallics*, 2022, **41**, 2119–2131.
22 D. A. Park, S. Byun, J. Y. Ryu, J. Lee, J. Lee and S. Hong, *ACS Catal.*, 2020, **10**, 5443–5453.
23 S. Zhou and C. Chen, *Sci. Bull.*, 2018, **63**, 441–445.
24 L. Guo, S. Dai, X. Sui and C. Chen, *ACS Catal.*, 2016, **6**, 428–441.
25 C. Chen, S. Luo and R. F. Jordan, *J. Am. Chem. Soc.*, 2008, **130**, 12892–12893.
26 M. Khoshsefat, Y. Ma and W. Sun, *Coord. Chem. Rev.*, 2021, **434**, 213788.
27 D. Laws, C. D. Poff, E. M. Heyboer and S. B. Blakey, *Chem. Soc. Rev.*, 2023, **52**, 6003–6030.
28 D. Peng, H. He, W. Pang, S. Behzadi and M. Qasim, *Polymer*, 2023, **280**, 126019.
29 Y. Zhang, H. Mu, L. Pan, X. Wang and Y. Li, *ACS Catal.*, 2018, **8**, 5963–5976.
30 G. Ren, R. Yuan, Q. Mahmood, Y. Zeng, Y. Wang, Z. Hu, S. Zou, T. Liang and W. Sun, *J. Mol. Struct.*, 2024, **1316**, 139037.
31 Z. Chen and M. Brookhart, *Acc. Chem. Res.*, 2018, **51**, 1831–1839.
32 F. Lin, M. Voccia, L. Odenwald, I. Göttker-Schnetmann, L. Falivene, L. Caporaso and S. Mecking, *J. Am. Chem. Soc.*, 2023, **145**, 27950–27957.
33 L. Min, W. Xingbao, L. Yi and C. Changle, *Angew. Chem., Int. Ed.*, 2017, **56**, 11604–11609.
34 Z. Lu, X. Xu, Y. Luo, S. He, W. Fan and S. Dai, *ACS Catal.*, 2023, **13**, 725–734.
35 J. Sun, M. Chen, G. Luo, C. Chen and Y. Luo, *Organometallics*, 2019, **38**, 638–646.
36 M. Janeta, J. X. Heidlas, O. Daugulis and M. Brookhart, *Angew. Chem., Int. Ed.*, 2020, **60**, 4566–4569.
37 Q. H. Tran, M. Brookhart and O. Daugulis, *J. Am. Chem. Soc.*, 2020, **142**, 7198–7206.
38 Q. Li, H. Mu and Z. Jian, *Polym. Chem.*, 2023, **14**, 3196–3202.
39 C. Chen, *Nat. Rev. Chem.*, 2018, **2**, 6–14.
40 S. Xiong, M. M. Shoshani, X. Zhang, H. A. Spinney, A. J. Nett, B. S. Henderson, T. F. Miller and T. Agapie, *J. Am. Chem. Soc.*, 2021, **143**, 6516–6527.
41 F. Ölscher, I. Göttker-Schnetmann, V. Monteil and S. Mecking, *J. Am. Chem. Soc.*, 2015, **137**, 14819–14828.
42 A. Michalak and T. Ziegler, *J. Am. Chem. Soc.*, 2001, **123**, 12266–12278.
43 H. Mu, G. Zhou, X. Hu and Z. Jian, *Coord. Chem. Rev.*, 2021, **435**, 213802.
44 S. Xiong, A. Hong, B. C. Bailey, H. A. Spinney, T. D. Senecal, H. Bailey and T. Agapie, *Angew. Chem., Int. Ed.*, 2022, **61**, e202206637.
45 S. Xiong, P. Ghana, B. C. Bailey, H. A. Spinney, B. S. Henderson, M. R. Espinosa and T. Agapie, *ACS Catal.*, 2023, **13**, 5000–5006.
46 M. J. Frisch, G. W. Trucks, H. B. Schlegel, G. E. Scuseria, M. A. Robb, J. R. Cheeseman, G. Scalmani, V. Barone, G. A. Petersson, H. Nakatsuji, X. Li, M. Caricato, A. V. Marenich, J. Bloino, B. G. Janesko, R. Gomperts, B. Mennucci, H. P. Hratchian, J. V. Ortiz, A. F. Izmaylov, J. L. Sonnenberg, D. Williams-Young, F. Ding, F. Lipparini, F. Egidi, J. Goings, B. Peng, A. Petrone, T. Henderson,

D. Ranasinghe, V. G. Zakrzewski, J. Gao, N. Rega, G. Zheng, W. Liang, M. Hada, M. Ehara, K. Toyota, R. Fukuda, J. Hasegawa, M. Ishida, T. Nakajima, Y. Honda, O. Kitao, H. Nakai, T. Vreven, K. Throssell, J. A. Montgomery Jr., J. E. Peralta, F. Ogliaro, M. J. Bearpark, J. J. Heyd, E. N. Brothers, K. N. Kudin, V. N. Staroverov, T. A. Keith, R. Kobayashi, J. Normand, K. Raghavachari, A. P. Rendell, J. C. Burant, S. S. Iyengar, J. Tomasi, M. Cossi, J. M. Millam, M. Klene, C. Adamo, R. Cammi, J. W. Ochterski, R. L. Martin, K. Morokuma, O. Farkas, J. B. Foresman and D. J. Fox, Gaussian 16 revision A.03, Gaussian, Inc, Wallingford, CT.

47 J. Tao, J. P. Perdew, V. N. Staroverov and G. E. Scuseria, *Phys. Rev. Lett.*, 2003, **91**, 146401.

48 P. J. Hay and W. R. Wadt, *J. Chem. Phys.*, 1985, **82**, 270–283.

49 W. R. Wadt and P. J. Hay, *J. Chem. Phys.*, 1985, **82**, 284–298.

50 P. J. Hay and W. R. Wadt, *J. Chem. Phys.*, 1985, **82**, 299–310.

51 S. Grimme, S. Ehrlich and L. Goerigk, *J. Comput. Chem.*, 2011, **32**, 1456–1465.

52 F. Weigend, *Phys. Chem. Chem. Phys.*, 2006, **8**, 1057–1065.

53 F. Weigend and R. Ahlrichs, *Phys. Chem. Chem. Phys.*, 2005, **7**, 3297–3305.

54 A. V. Marenich, C. J. Cramer and D. G. Truhlar, *J. Phys. Chem. B*, 2009, **113**, 4538–4543.

55 E. R. Johnson, S. Keinan, P. Mori-Sánchez, J. Contreras-García, A. J. Cohen and W. Yang, *J. Am. Chem. Soc.*, 2010, **132**, 6498–6506.

56 T. Lu and F. Chen, *J. Comput. Chem.*, 2012, **33**, 580–592.

57 T. Lu, *J. Chem. Phys.*, 2024, **161**, 082503.

58 W. Humphrey, A. Dalke and K. Schulten, *J. Mol. Graphics*, 1996, **14**, 33–38.

59 C. Y. Legault, *CYLview20*, Université de Sherbrooke, 2020, https://www.cylview.org.

60 S. Noda, A. Nakamura, T. Kochi, L. W. Chung, K. Morokuma and K. Nozaki, *J. Am. Chem. Soc.*, 2009, **131**, 14088–14100.

61 E. Rezabal, J. M. Ugalde and G. Frenking, *J. Phys. Chem. A*, 2017, **121**, 7709–7716.

62 D. Guironnet, L. Caporaso, B. Neuwald, I. Göttker-Schnetmann, L. Cavallo and S. Mecking, *J. Am. Chem. Soc.*, 2010, **132**, 4418–4426.

63 N. Ryo, C. L. Wa, W. Yumiko, O. Yoshishige, O. Yoshikuni, I. Shingo, M. Keiji and N. Kyoko, *ACS Catal.*, 2016, **6**, 6101–6113.

64 Z. Song, S. Wang, R. Gao, Y. Wang, Q. Gou, G. Zheng, H. Feng, G. Fan and J. Lai, *Polymers*, 2023, **15**, 4343.

65 Z. Chen, W. Liu, O. Daugulis and M. Brookhart, *J. Am. Chem. Soc.*, 2016, **138**, 16120.

66 S. Mecking, L. K. Johnson, L. Wang and M. Brookhart, *J. Am. Chem. Soc.*, 1998, **120**, 888–899.

67 W. Tian, H. Guan, W. Wang, X. Kong, W. Pang, Q. Wang, F. Wang and C. Zou, *Appl. Organomet. Chem.*, 2025, **39**, e70063.

68 J. Tan, J. Liu and X. Zhang, *J. Org. Chem.*, 2025, **90**, 2052–2061.

69 R. G. Pearson, *Inorg. Chem.*, 1988, **27**, 734–740.

70 P. Geerlings, F. De Proft and W. Langenaeker, *Chem. Rev.*, 2003, **103**, 1793–1874.